From design to evaluation of an additively manufactured, lightweight, deployable mirror for Earth observation

Marcell Westsik, James T. Wells, Younes Chahid, Katherine Morris, Maria Milanova, Mat Beardsley, Michael Harris, Lucas Ward, Simon G. Alcock, Ioana-Theodora Nistea, Simone Cottarelli, Samuel Tammas-Williams, and Carolyn Atkins

Published version information:

Citation: Marcell Westsik, James T. Wells, Younes Chahid, Katherine Morris, Maria Milanova, Mat Beardsley, Michael Harris, Lucas Ward, Simon G. Alcock, Ioana-Theodora Nistea, Simone Cottarelli, Samuel Tammas-Williams, Carolyn Atkins, "From design to evaluation of an additively manufactured, lightweight, deployable mirror for Earth observation," Proc. SPIE 12677, Astronomical Optics: Design, Manufacture, and Test of Space and Ground Systems IV, 1267704 (4 October 2023)

DOI: https://doi.org/10.1117/12.2677303

PROCEEDINGS OF SPIE

SPIEDigitalLibrary.org/conference-proceedings-of-spie

From design to evaluation of an additively manufactured, lightweight, deployable mirror for Earth observation

Marcell Westsik, James Wells, Younes Chahid, Katherine Morris, Maria Milanova, et al.

Marcell Westsik, James T. Wells, Younes Chahid, Katherine Morris, Maria Milanova, Mat Beardsley, Michael Harris, Lucas Ward, Simon G. Alcock, Ioana-Theodora Nistea, Simone Cottarelli, Samuel Tammas-Williams, Carolyn Atkins, "From design to evaluation of an additively manufactured, lightweight, deployable mirror for Earth observation," Proc. SPIE 12677, Astronomical Optics: Design, Manufacture, and Test of Space and Ground Systems IV, 1267704 (4 October 2023); doi: 10.1117/12.2677303

SPIE.

Event: SPIE Optical Engineering + Applications, 2023, San Diego, California, United States

From design to evaluation of an additively manufactured, lightweight, deployable mirror for Earth observation

Marcell Westsik*[a], James T. Wells[a], Younes Chahid[a], Katherine Morris[a], Maria Milanova[a], Mat Beardsley[b], Michael Harris[b], Lucas Ward[b], Simon G. Alcock[c], Ioana-Theodora Nistea[c], Simone Cottarelli[d], Samuel Tammas-Williams[d], and Carolyn Atkins**[a]

[a]UK Astronomy and Technology Centre, Royal Observatory, Edinburgh, EH9 3HJ, UK
[b]RAL Space, Harwell Science & Innovation Campus, OX11 0QX, UK
[c]Diamond Light Source, Harwell Science & Innovation Campus, OX11 0QX, UK
[d]School of Engineering, University of Edinburgh, Edinburgh, EH9 3FB, UK

ABSTRACT

Additive manufacturing (AM; 3D Printing) is a process that fabricates objects layer-by-layer, unlocking previously unachievable geometrical freedom in design and manufacture. Its adoption for the manufacture of optical components for nanosats is challenging due to limited understanding of its inherent porosity and outgassing properties; however, AM has plenty of potential for lightweight space-based mirror structures as it enables the use of lattice structures and topology optimisation. AM is particularly relevant to nanosat deployable optics (DO) instrumentation, where a segmented mirror needs to be packed within a limited volume and mass budget. This paper describes the design, analysis, manufacture and metrology of AM mirror petal prototypes for a 6U nanosat DO payload. The objective of the prototypes was to reduce the mass and the part count relative to the conventional design. From the available 33 volumetric lattices including graph, triply periodic minimal surface and stochastic lattices within the AM design software used, two were downselected by using finite element analysis and manufacturability experiments. Prototypes were designed using these lattices, and the geometric and interface requirements of the conventional petal. These were printed, using laser powder bed fusion, in the aluminium alloy AlSi10Mg and post-processed using single point diamond turning. The internal (porosity) and external geometrical properties of the manufactured prototypes were measured using X-ray computed tomography and the optical properties of the reflective surface evaluated using interferometry. By utilising AM, a mass reduction of 44 % and the consolidation of nine parts into one was achieved.

Keywords: Additive manufacturing, 3D printing, mirror fabrication, lightweight metal mirrors, lattices, topology optimisation, metrology

1. INTRODUCTION

In recent years, Additive Manufacturing (AM; 3D printing) has been the focus of many lightweight mirror research projects which can be attributed to the numerous unique benefits of this technology that conventional manufacturing cannot provide. AM fabricates an object layer-by-layer, and hence provides an unparalleled design freedom compared to conventional subtractive manufacturing which enables designers to envision novel ways in which the mass of the mirror can be reduced; a crucial consideration for space-based optics. These novel ways of mass reduction may include using lattice structures, topology optimisation and part consolidation.[1] Lattice structures are used to fill internal volumes and maintain some of the original structural strength. There are three main categories of volumetric lattices researched in this field: graph lattices, skeletal and sheet based Triply Periodic Minimum Surface (TPMS) lattices, and stochastic lattices. Graph lattices are strut-based periodic lattices (Figure 1a). TPMS lattices are equation driven and also periodic lattices, they produce continuous surfaces when constructed with either struts or walls, which are self-supporting in any build orientation, making them ideal for AM (Figure 1b). Stochastic lattices are randomized, non-periodic structures constructed with

*E-mail: mwestsik.research@gmail.com
*E-mail: carolyn.atkins@stfc.ac.uk

Astronomical Optics: Design, Manufacture, and Test of Space and Ground Systems IV,
edited by Tony B. Hull, Daewook Kim, Pascal Hallibert, Proc. of SPIE Vol. 12677,
1267704 · © 2023 SPIE · 0277-786X · doi: 10.1117/12.2677303

struts (Figure 1c). Topology optimisation can be used to determine the optimal design shape according to the particular design volume, load case and optimisation objective.

The most researched AM method used for lightweight mirrors is Laser Powder Bed Fusion (L-PBF) which utilises high power laser to locally melt metal powder layer-by-layer to construct the final part.[2] Current state-of-the-art space-based mirrors are either open-back, used on the *James Webb Space Telescope*,[3] or sandwich structures, used on the *Hubble Space Telescope*.[4] Open-back mirrors have less structural efficiency but are quicker and lower cost to manufacture, whilst sandwich mirrors possess increased structural efficiency at the expense of a time consuming manufacturing and assembly process and, therefore, higher cost.[2] Adopting AM for the manufacture of space mirrors makes combining the benefits of the open-back and sandwich design possible by printing sandwich structures in a single step, hence negating the need for assembly, reducing lead time, and providing good structural efficiency. On the other hand, the use of AM introduces unique challenges with design[5] and post-processing,[6] and the outgassing properties of such components.[7]

(a) Graph lattice (Fluorite) (b) Walled TPMS lattice (Gyroid) (c) Stochastic lattice (Voronoi)

Figure 1: Three main lattice categories: graph, walled TPMS and stochastic. Within these main categories there are numerous different types of lattices available, discussed in Section 3.1.

Challenges encountered and overcome in previous work include connectivity of internal volumes for powder removal,[8] self-supporting lattice structures and quilting effects,[5] isolating screw pressure induced by mounting from the optical surface,[9] porosity beneath the mirror substrate[6] affecting the results of Single Point Diamond Turning[10] (SPDT) which increases scattering. Lightweighting of mirrors has been achieved by utilising beam-based periodic lattice structures[5],[11] 2-D foam and volumetric Voronoi stochastic lattice structures[12],[13] and optimising them using topology optimisation. The latter research mainly focused on the thermal properties of the latticed mirror design with little detailing of the optical performance under post-processing loading conditions. In previous research, ten types of lattice structures' mechanical properties were experimentally analysed at four different relative densities per lattice, including graph, skeletal and walled TPMS lattices.[14] It was found that, in general, walled TPMS lattices possess the highest Young's moduli out of the three main lattice categories; strut-based lattices being the second best. The printability of struts at different inclination angles and bridging lengths was studied by Meyer et al.,[15] which is relevant to selecting build orientation and unit cell size for graph lattice structures.

In the AM design software used for this research, nTopology, many new lattices were available with little overlap between previously analysed lattices, such as some graph lattices, TPMS lattices and stochastic lattices - as shown in Figure 1. Their quilting properties are analysed in this project to determine how suitable they are for mirror lightweighting. Powder removal is also an important consideration in designing latticed AM parts due to optimum lightweighting and health and safety implications - for example, metal powders are flammable and due to their grain size (15 - 45 microns) have the potential for respiratory and cutaneous irritation.[16] Powder removal properties of semi-enclosed lattices available within the AM design software have not been documented in open literature before, therefore in this study these will be analysed. Many AM mirror research papers are limited to strut-based lattices and lack part consolidation. Hence, this research project will combine part consolidation, latticing and topology optimisation within a single design.

The AM prototype design was based on one of the two rectangular M1 mirror petals, highlighted in Figure 2, in the deployable optics payload developed within the Integrated Space Active Optics for Aberration Compensation (ISAAC) project at the UK Astronomy Technology Centre (UK ATC).[17] The AM design software was used to generate lattice structures for structural lightweighting and to perform topology optimisation for part consolidation and design optimisation. From the 33 available volumetric lattices in the software, four were selected using automated Finite Element Analysis (FEA) simulations. Then, these four lattices were evaluated by performing powder removal experiments at two different weight remaining (WR) values using Stereolithography (SLA) printed lattice samples, detailed in Section 3.1. The WR value is defined by the following equation:

$$WR = \frac{\text{Mass of lattice}}{\text{Mass of latticed volume}}$$

The AM petal prototypes were finalised based on the results of the lattice downselection process, design and manufacturing constraints, and iterative design optimisations, detailed in Section 3. Four prototypes were printed using an industrial L-PBF printer in AlSi10Mg material, two with graph latticing and two with walled TPMS latticing, shown in Section 4. Further two samples were printed using an academic L-PBF printer operated by the Henry Royce Institute (HRI) in the material AlSi10Mg. Some of the prototypes were either Single Point Diamond Turned (SPDT) at the Rutherford Appleton Laboratory (RAL Space), Section 5, or evaluated using X-ray Computer Tomography (X-ray CT) at the National Physical Laboratory (NPL), Section 6.4. The SPDT surface was optically evaluated for surface micro roughness using white light micro-interferometry at Diamond Light Source (DLS), detailed in Section 6.3.

2. MIRROR DESIGN SPECIFICATION

2.1 ISAAC deployable mirror assembly

The main dimensions of the prototype were defined by the original M1 side mirror from the ISAAC deployable optics assembly. This telescope is developed to bridge the gap between expensive and high resolution, and low-cost and low resolution Earth observation (EO) satellites by fitting a segmented $\geq 30\,\text{cm}$ diameter M1 mirror within a 6U CubeSat, where one U represents a volume of $10 \times 10 \times 10\,\text{cm}$. The resulting system would provide a ground sampling distance $\leq 1\,\text{m}$ in the visible spectrum and would be ideal for EO satellite constellations. The deployable primary mirror fits within a 4U volume, $10 \times 20 \times 20\,\text{cm}$, and has a mass of 1548 g. The petal to be re-designed has nominal dimensions of $191.5 \times 106 \times 42\,\text{mm}$, it is constructed from 9 components and has a combined mass of 437 g.

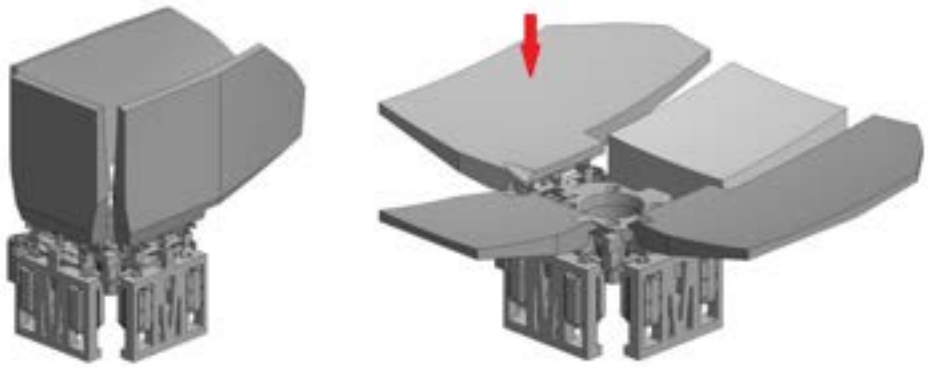

Figure 2: ISAAC deployable M1 assembly in stowed and deployed configuration.[17]

2.2 Prototype Mirror design requirements

Figure 2 shows the telescope in stowed and deployed states; the highlighted petal is to be re-designed for AM in this study. The objectives of the re-design process were to develop an AM optimised mirror petal which

is compliant with the ISAAC petal's geometrical requirements, to incorporate lightweighting features and part consolidation, and to explore the design freedom and manufacturability through the process. There were no optical requirements on form error and roughness. The requirements are summarised in Table 1.

Table 1: Prototype design requirements.

Requirement type	Parameter	Specification
Optical	optical prescription radius of curvature (ROC)	spherical, concave 682.28 mm
Mechanical	mirror substrate thickness mounting features weight reduction	1 mm 3 ∗ M3 tooling ball 50 %
	The AM design shall conform geometrically to the original assembly.	
AM	material minimum wall thickness support structures powder removal	Aluminium (AlSi10Mg desired) 0.8 mm internal support structures shall be avoided all powder shall be removed
Machining	extra material on mirror substrate extra feature on mirror substrate mounting features	1.0–1.5 mm 1.25–1.75 mm chamfer 3 ∗ M4 SPDT mounts 3 ∗ stand-offs for clamping

2.3 AM design considerations

The use of AM imposes limitations which need to be addressed during the design process, these are the following.

- Lattice choice - Lattices are beneficial structures for weight reduction due to their variety and customizability. These structures can be found in nature, such as foam lattices in trabecular bones, honeycomb lattices in bee hives and wasp nests, and crystal structures. The lattice choice affects the quilting and powder removal properties, and the structural strength of the component.
- Print orientation - The selected printing orientation influences the optimal orientation of graph lattices, and the geometry and location of escape holes for powder removal. It is desired to avoid overhangs below 45 degrees relative to the build plate and large unsupported horizontally overhanging surfaces with L-PBF due to increased surface roughness,[15] and increased risk of de-lamination and print failures. Moreover, increased surface roughness can affect the outgassing rate.[7]
- Powder removal - During the L-PBF process, unmelted powder is entrapped within the empty regions of the component; this residual powder needs to be removed before the component can be separated from the build plate. This consideration influences the overall design of the component and imposes limitations on the suitable lattices.
- Post-machining - Numerous features of the printed component need to be machined to attain the desired geometric accuracy using Computer Numeric Control (CNC) milling, CNC turning and SPDT. To make these processes feasible, extra features need to be included for clamping, mounting and positioning.

2.4 Process chain

Once the requirements were understood, the lattices were downselected with the AM design software's inbuilt FEA tool and command line interface, and combined with a custom Python script to automate the pre- and post-processing stages of the simulations. Autodesk Inventor was used to model the conventional CAD files. These files were then imported into the AM design software for latticing and topology optimisation to generate the AM design. Once finalised, the AM design was surface meshed within the AM software and exported as a .STL file. FEA studies were run with two different loading conditions on the prototype using the AM design

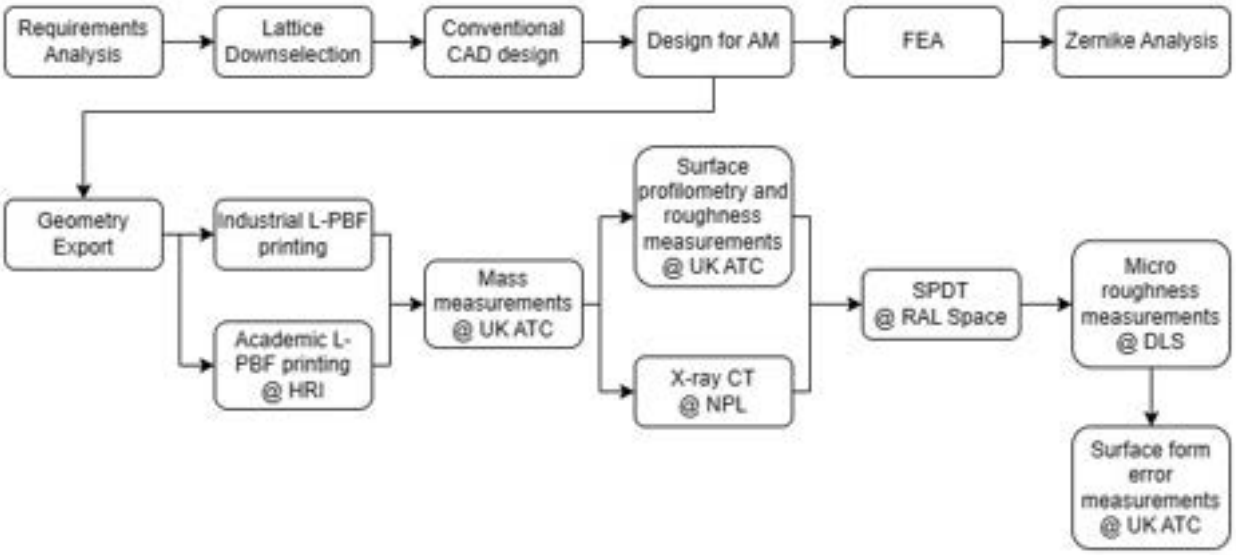

Figure 3: Prototype design, manufacturing and evaluation flow chart.

software's inbuilt FEA tool, the displacement point maps were exported for performing Zernike analyses using a custom MATLAB script.

Once the printed samples were received, the weight of all four and the surface roughness and surface profile of two prototypes were measured at the UK ATC. Two samples were sent to RAL Space for SPDT. The remaining two samples were sent to the National Physics Laboratory (NPL) to be measured via X-ray CT before being sent to SPDT. The micro roughness of the diamond turned samples was measured at DLS. As the final step, the form error of the prototypes was evaluated at the UKATC. Figure 3 visualizes the processing steps from design to evaluation.

3. DESIGN PROCESS

3.1 Lattice downselection

The AM design software used enables the development of periodic and stochastic volumetric lattices. Periodic volumetric lattices can be created from 23 Graph and 6 TPMS unit cells. Stochastic lattices can be created using 4 separate approaches, all of which rely on point clouds.

The first stage of the downselection process differed between the periodic and stochastic lattices. For the periodic lattices, this stage focused on the manufacturability of the available unit cells and its criteria included available printing orientations, lengths of overhanging elements and enclosed volumes. For the stochastic lattices, their previous recorded applications and the algorithms behind their generation was considered, that is, how well understood their mechanical behaviour is.

The second and third stage of the downselection process focused on the mechanical behaviour of the lattices at a range of WR values. Limited information on the mechanical properties of some of these lattices is available in the literature,[14] however, to compare every downselected lattice, it was necessary to perform FEA on each one of them. The WR value was controlled by fixing the unit cell size for the periodic lattices and modifying the beam or wall thickness from a minimum of 0.8 mm to a thickness corresponding to 50 % WR. The minimum thickness was determined by the minimum allowable feature size corresponding to the AM machines used. The WR value of the downselected stochastic lattice was controlled by varying the point spacing of the generated point cloud and fixing the beam thickness at 1 mm. The stages of the downselection process and each lattice examined are summarised in Figure 4.

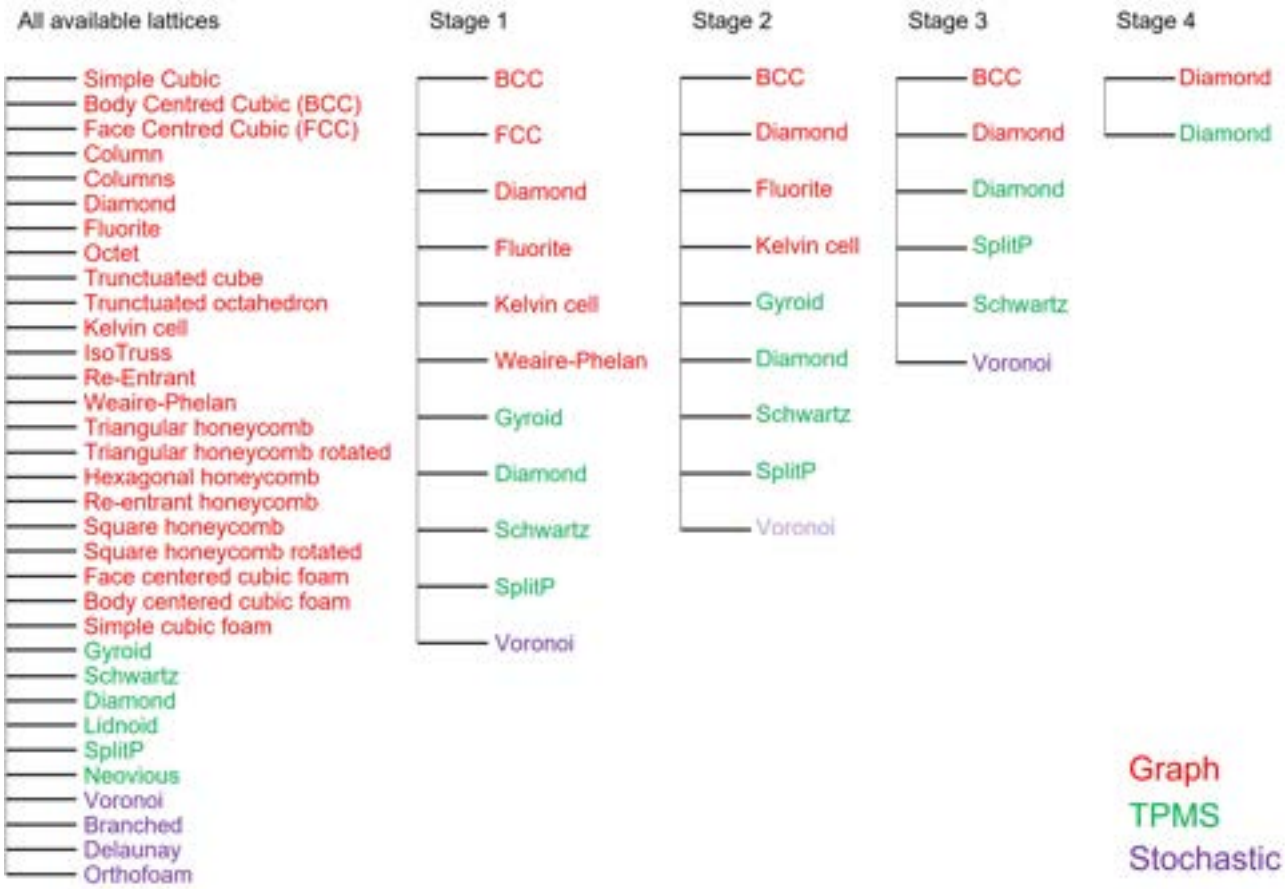

Figure 4: Lattice downselection process stages.

40×40 mm sandwich samples were created within the AM design software with 1 mm thick solid layers on top and bottom, and a 10 mm tall latticing volume. A unit cell size of $10 \times 10 \times 10$ mm was used with a beam/wall thickness of 1 mm; 16 unit cells included in every sample. Pictures defining the sandwich sample geometries can be seen in Figure 5.

(a) Graph Diamond sandwich structure

(b) TPMS Diamond sandwich structure

(c) Voronoi sandwich structure

Figure 5: Lattice downselection example sample geometries.

Three loading conditions were examined: a pressure load, lateral and twisting force loads. Identical restraints were applied in all loading conditions; all nodes on the base of the sample were restrained in translation and rotation in x, y and z. Pictures of the loading conditions with corresponding deformation shapes can be seen in Figure 6 for the Body Centred Cubic (BCC) unit cell. The pre-set AlSi10Mg material properties were used for the study.

The results of the simulations are summarised in Figures 7 and 8. Initial simulations on the TPMS lattices

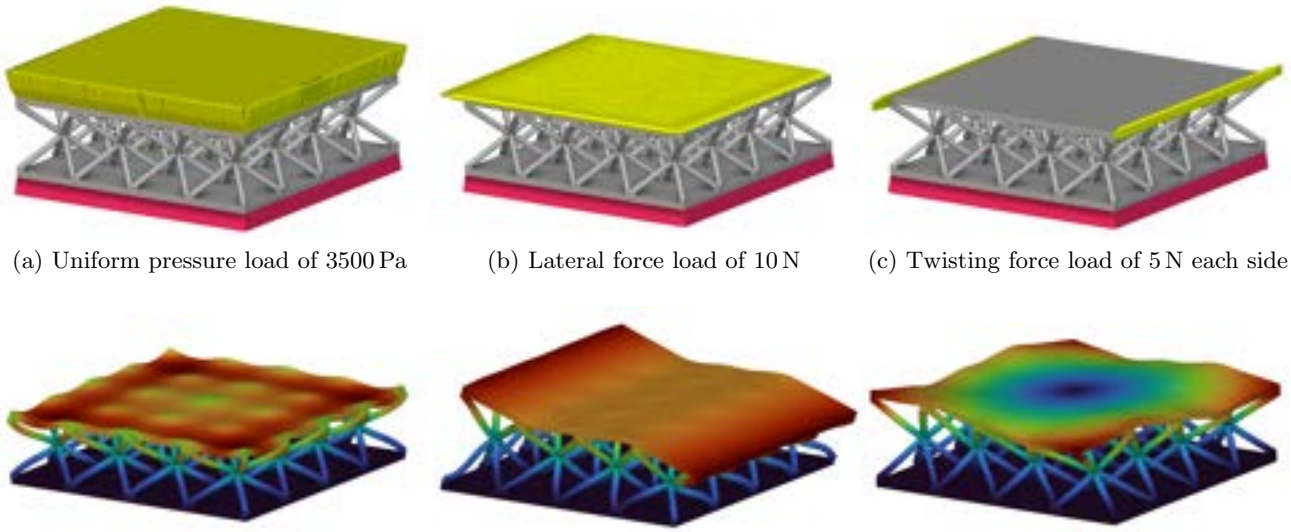

(a) Uniform pressure load of 3500 Pa (b) Lateral force load of 10 N (c) Twisting force load of 5 N each side

(d) Perpendicular deformation shape (e) Lateral deformation shape (f) Twisting deformation shape

Figure 6: Lattice downselection FEA load cases and deflection shapes.

were performed by using non-exact thickness representations, which resulted in actual wall thicknesses below the desired value but could be generated at a lower computational cost. Once displacement data was gathered in a large WR range with the non-exact thickness lattices, exact thickness representations were used for the Diamond TPMS lattice in the close range of the selected WR design point. The results of these simulations are featured as TPMS Diamond and TPMS Diamond exact thickness on the plots. Based on the simulation results, their mechanical properties were found to be nearly identical. Due to limitations in computing power, Voronoi lattices could not be simulated using solid elements above the WR value of 17.91 %. In order to estimate their mechanical properties at higher WR values, beam element simulations were undertaken, which provided significantly different results to the solid element simulations for identical geometries. The results of the two separate simulation methods are featured in the figures as Voronoi Solid and Voronoi Beam.

The results presented in Figures 7a, 7b and 8a show that the TPMS lattices perform better than or identically to the graph lattices for the same WR values under each loading condition and in every displacement metric. However, they cannot be generated for WR values lower than 17.4 % using non-exact thickness representations. Due to the limitations in time and computing power, only the TPMS Diamond lattice was simulated with exact thickness representations, and its resulting properties match closely those of the non-exact thickness representation. Graph lattices can be used with WR values down to 2.8 % but the resulting surface displacement will be large. At higher WR values, the displacement properties of the graph lattices converge to and often match the properties of the TPMS lattices. The Voronoi lattice's displacement properties, based on results from simulations using solid elements in the WR range of 6.3 % - 17.9 %, can be better than those of the Graph lattices under the perpendicular loading condition for Minimum and Average displacement values. On the other hand, it performs similarly to or worse than the graph lattices under other load cases and with different displacement metrics.

Since outgassing is a consideration for space applications, and it correlates with surface area,[7] the surface area of a $10 \times 10 \times 10$ mm unit cell of each downselected lattice type was determined and plotted in Figure 8b. As outgassing correlates with surface area, it is desired to use lattices with minimal surface area. Figure 8b shows that in graph lattices possess smaller surface area than TPMS lattices for identical WR values. Between the graph lattices, the graph Diamond has smaller surface area than the BCC. Comparing the TPMS lattices, the SplitP lattice has the largest surface area per unit cell, with the TPMS Diamond following. The TPMS Schwartz lattice has the smallest surface area in this lattice category. It is worth taking note of the growth trends in surface area with WR for each lattice category. While the stochastic Voronoi lattice's surface area steadily increases with WR, the graph lattices' surface area seems to initially increase in the region of 4 % - 30 % and then level out or decrease, depending on the lattice type. The TPMS lattices' surface area decreases with

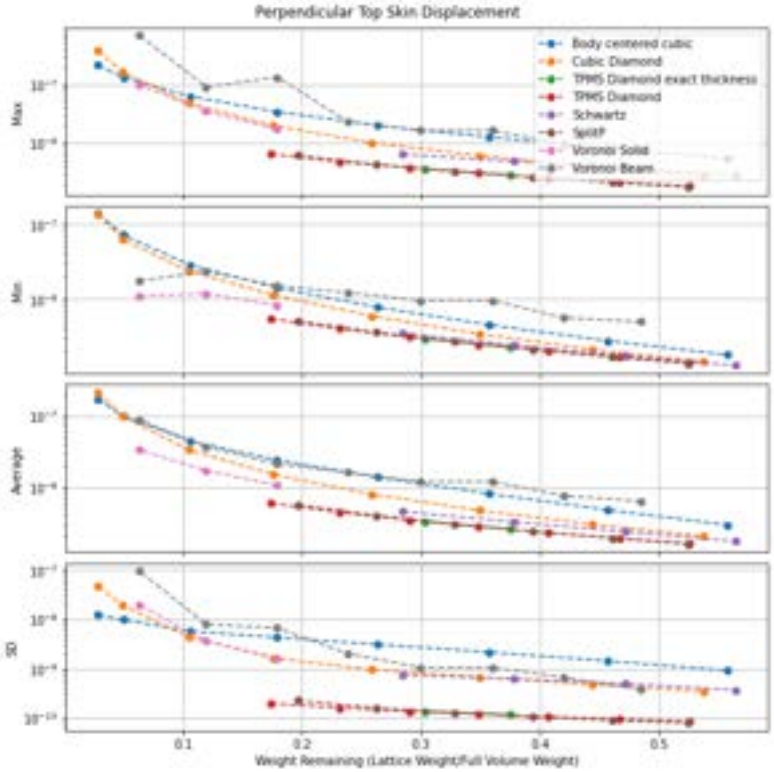

(a) Lattice perpendicular displacement properties

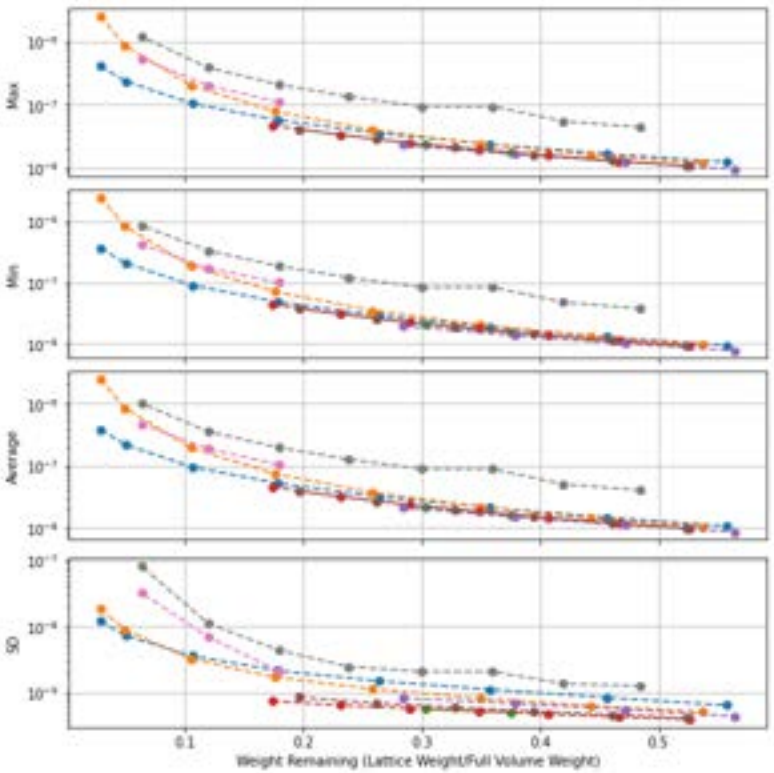

(b) Lattice lateral displacement properties

Figure 7: Lattice properties result set No. 1.

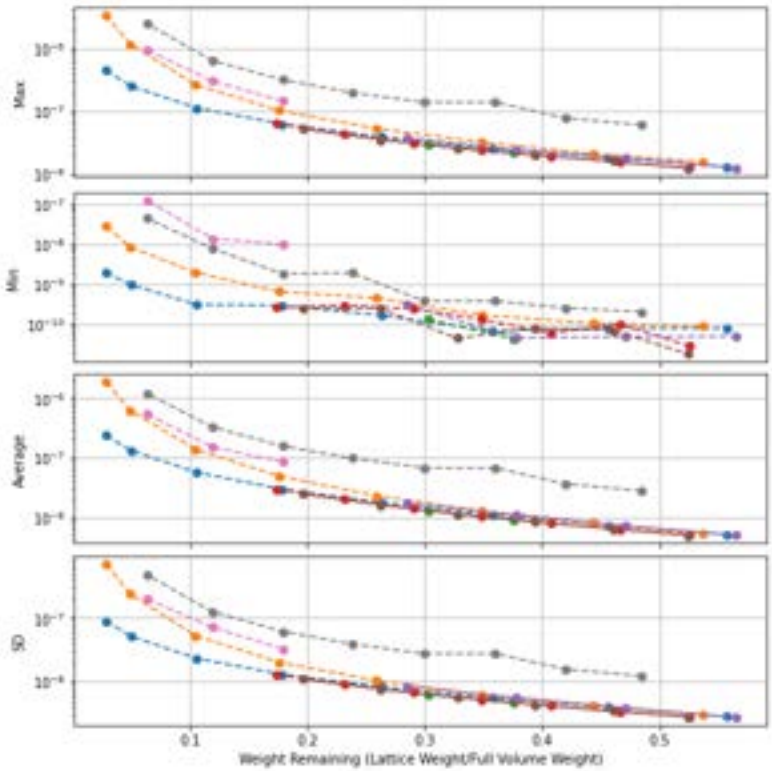

(a) Lattice twisting displacement properties

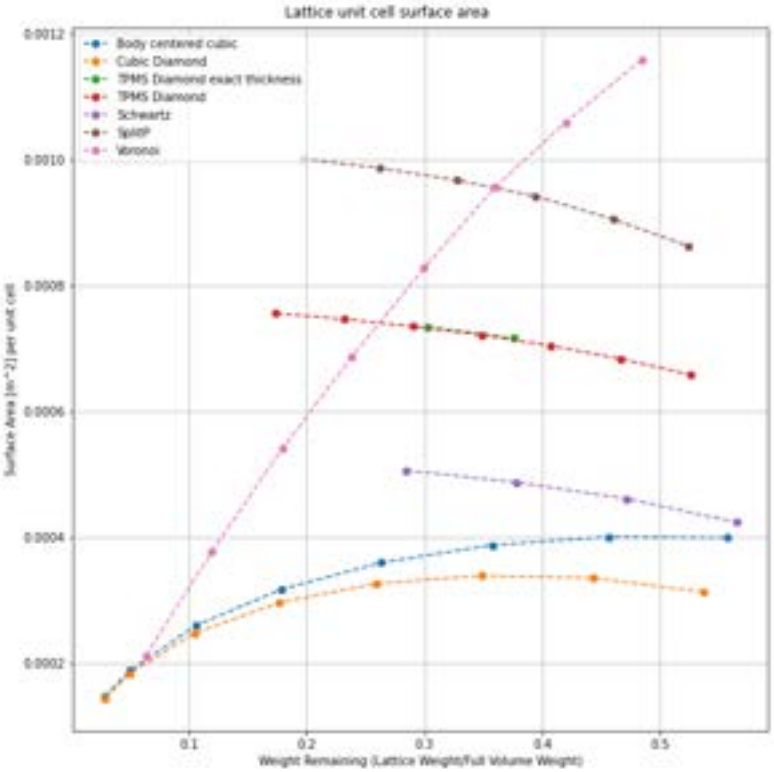

(b) Lattice unit cell surface area properties

Figure 8: Lattice properties result set No. 2.

increasing WR value.

Based on these findings, the graph BCC and Diamond, and TPMS Diamond and SplitP lattices were selected for further, experimental, investigations in stage four of the downselection process. This resulted in the selection of the Graph Diamond and TPMS Diamond lattices for the final petal designs. The details of these experiments are discussed in Section 3.2.1.

3.2 Powder removal experiments

Two sets of powder removal experiments were carried out during the design process. Firstly, experiments were performed to aid the lattice downselection process, and, secondly, to inform decisions on the optimal location and the number of powder escape holes on the prototypes. Instead of metal AM powder, however, red coloured sand was used to eliminate health risks and increase visibility of the medium.

3.2.1 Powder removal experiments - Lattice downselection

No literature was found on the powder removal properties of lattices available in the AM design software, therefore it was necessary to perform custom experiments on the most promising downselected lattices. A sample geometry modeling the main features of a mirror was developed, incorporating a spherical face with conformal latticing, a latticing volume height ranging from 5 mm to 10 mm, and two escape holes next to corners in different sizes. These samples were manufactured using SLA with ClearVue material by an external bureau. Table 2 showcases the lattices and WR values used within the test samples, and Figure 9 provides pictures of the BCC 50 % sample.

Table 2: Powder Removal Experiment - Lattice downselection samples.

Lattice Category	Lattice Type	WR Value [%]
Graph	BCC Diamond	25, 50
TPMS	SplitP Diamond	

The results of the tests give a qualitative assessment of the powder removal properties of different lattices at different WR values. The mass of each sample was measured before and after the test in order to determine the residual sand within the sample, however, the mass of the residual sand did not appear to correlate with geometry. It was advised that after the SLA printing process, the lacquer used to provide a transparent surface finish on the outer surfaces of the samples, might have entered the lattice structure and increased the 'stickiness' of the lattice resulting in larger mass of residual sand. However, the videos of the sand removal process provided valuable insights into the ease with which powder can be removed from the lattice structures.

It was found that between the graph lattices, the Diamond performed better than the BCC as it provides small resistance flow-paths in parallel and diagonal directions, whereas the BCC only has small resistance flow-paths in the parallel directions. A picture taken of the Graph Diamond 25 % WR lattice mid-experiment is featured in Figure 10.

When examining the TPMS lattices, the Diamond lattice had superior removal capabilities as it provides clear flow-paths in the diagonal directions, making powder removal relatively easy when compared to the SplitP lattice. No clear flow-paths were found for the SplitP lattices.

It should be noted, that all samples could be fully filled with sand which could be fully removed through the smallest escape hole, no entrapped sand was found. Residual sand was only present on the internal surfaces. A higher concentration of residual sand could be found in the vicinity of edges and corners, suggesting the use of fillets.

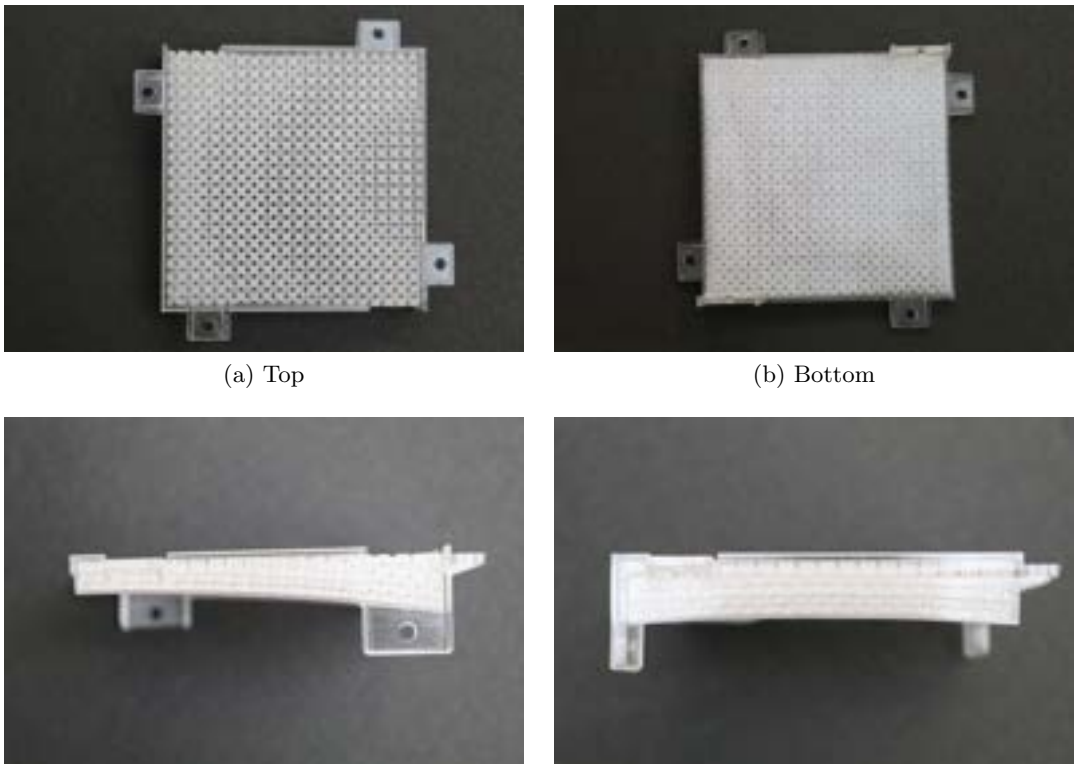

(a) Top (b) Bottom

(c) Side (d) Back

Figure 9: BCC 50 % WR lattice powder removal sample.

Figure 10: Lattice powder removal experiment - Graph Diamond 25 % WR.

3.2.2 Powder removal experiments - Prototype design

The geometry of the prototype design, the latticing cell size and WR value differs from the original powder removal experiment samples'. To increase confidence in the printability of the designs, an SLA sample was created based on the geometry of the TPMS design, which was expected to be a higher risk print in terms of powder removal. This sample was manufactured in the same way as the lattice powder removal samples, described in Section 3.2.1, pictures of the prototype sample are featured in Figure 11.

Multiple experiments were conducted and recorded with different open escape hole combinations, see Figure 12. It was found that all the sand could be removed from within the petal through the side opening by re-orienting and shaking the petal in multiple directions. However, after sharing the recordings of the experiment

(a) Prototype sample front (b) Prototype sample back

Figure 11: Prototype powder removal sample.

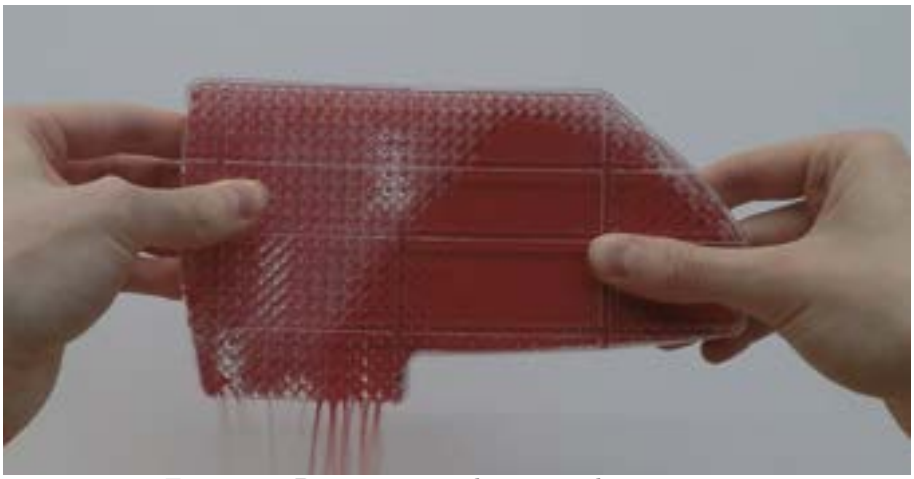

Figure 12: Prototype powder removal experiment.

and consulting with the AM bureau, it was decided to leave one escape hole open on the top side of the petal on the TPMS design. The Graph petal design was finalised with a single side opening.

3.3 Print orientation selection

The OPTICON A2IM Cookbook[2] provides detailed guidance on print orientation selection. Based on the included information, the printing orientations were selected to minimise overhanging areas and bridges. Overhanging surfaces below 45 degrees relative to the build plate exhibit considerably larger surface roughness[14,15] which might correlate with higher outgassing rates.[7] Therefore, graph lattices need to be oriented so that individual beams' overhang angle is maximised.

Previous research shows that the porosity in the vicinity of substrates is minimised when substrates are printed in a vertical orientation.[10] Minimising the porosity in said locations is critical for acceptable optical surface quality after SPDT.

When selecting printing orientation and designing a part for AM, it is also important to consider heat transfer throughout the L-PBF printing process, and to ensure that adequate heat escape paths are incorporated into the built part either via design or additional support structures. This is necessary, as residual heat during the printing process can cause considerable warping which can affect the geometrical accuracy of the part or cause print failure.

Another consideration when determining the printing orientation was the size of the build chamber on the AM machines to be used. One of the printers to be used is the Aconity3D AconityLab, which has a build volume

of Ø 170 mm x H 200 mm. This build volume only permits the manufacture of a petal in the upright position and made it necessary to rescale the prototype for printing.

Selecting the printing orientation provided design drivers for Design for AM (DfAM), through which features were optimised for respective printing orientations by avoiding overhangs smaller than 45 degrees relative to the build plate and cylindrical holes whose axis is below the same threshold. More information on DfAM can be found in Section 3.4. Furthermore, it was ensured that the remaining overhanging surfaces are adequately supported by the lattice structures within the prototype or supported by removable supports outside the prototype, also ensuring sufficient heat dissipation.

3.4 Final design

The lessons learned from the previous subsections were incorporated into the final prototype design. Based on the results of Section 3.1 and 3.2.1, the Graph Diamond and TPMS Diamond lattices were used to create two prototype designs. The results of Section 3.3 defined the orientation of the mounting features to be used for post-machining, set out in Section 2.2, and the shape of the tooling ball mounting features. Based on the work featured in Section 3.2.2, the shape of the prototype was validated for powder removal and the location of the necessary powder escape holes were determined. The simulated optical aberrations are detailed in Section 3.5.

During the design stage, DfAM best practices were followed. Some of these practices were incorporated into the prototype design requirements, in Section 2.2. Furthermore, during the design process it was ensured that the number and size of overhanging areas are minimized, heat dissipation is sufficient throughout the build, cylindrical holes are avoided, powder escape routes are added, extra material is added to post-machined surfaces and, where supports needed to be added, support removal is feasible. The SPDT mounts were orientated and designed to be self-supporting during printing and isolate some of the screw pressures during post-processing. They incorporate three screw holes and two dowel pin holes. The tooling ball mounts were designed so that they are self supporting for the TPMS version and isolate some of the screw pressure from the optical surface exerted by the tooling balls. The topology optimised tooling ball mount is optimised for stiffness and mass, and reduced the overall component count by five. The spring mounts were consolidated into the prototype. The main features of the graph prototype are highlighted in Figure 13 and the final latticed designs can be seen in Figure 14.

All edges of the prototypes were filleted to minimize thermally induced stress concentrations and the risk of cracks developing. Extra material of 1.5 mm was added to the tooling ball and SPDT mounts to be removed through post-machining, and 1.25 mm to the mirror surface to minimise porosity, based upon a study using the same printer and evaluating the frequency of porosity with distance from the external surface.[6]

3.5 Numerical simulations and Zernike analysis

Simulations were performed to understand the quilting effect caused by the SPDT process, and the distortions induced by the screws attached and/or removed after post-machining. Quilting is introduced into the system as any non-solid structure will imprint on to the optical surface in some capacity, which affects the optical quality. The affect of screws needs to be understood as tooling balls will be screwed into the part-consolidated areas of the prototype and will introduce some optical distortion. Furthermore, the prototype is attached via screws to the SPDT jig during post-machining and this inherently leads to some deformation of the three attachment points which is transferred to the optical surface. Once the screws are removed, the stresses leading to deformation vanish, leaving the prototype with an inversely distorted optical surface.[9] Ultimately, the goal of these studies is to predict what distortions might be seen on the interferometer and what might be redesigned in the future.

Simulations were performed with the FEA tool of the AM design software with solid elements. Attempts were made to export meshes and node sets from the AM software and perform the simulation setup, solving and post-processing in a dedicated simulation software package, however, this workflow led to issues with setting up the desired load cases. These issues could not be solved in the given time frame. After these attempts, one set of benchmark simulations was performed to validate the FEA accuracy of the AM design software in terms of displacement. The deformation of the BCC sandwich structure under the pressure load of 3500Pa was simulated in nTopology and Ansys Mechanical using the pre-set AlSi10Mg mechanical properties in both packages and identical meshes and boundary conditions. The results showed that between the maximum deflection results

(a) Protrusions on mirror face

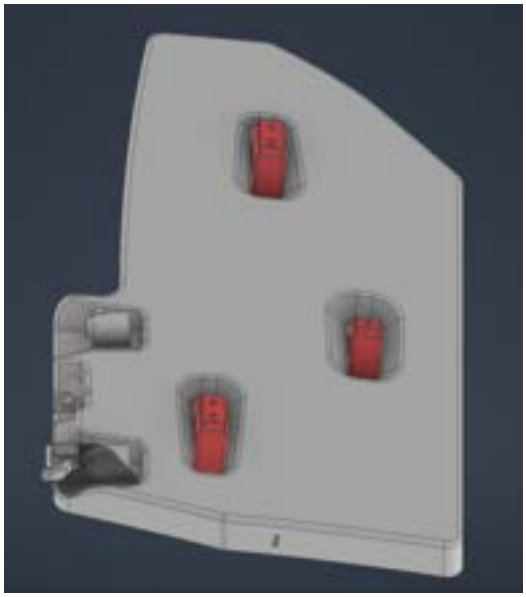

(b) SPDT mounts on back face

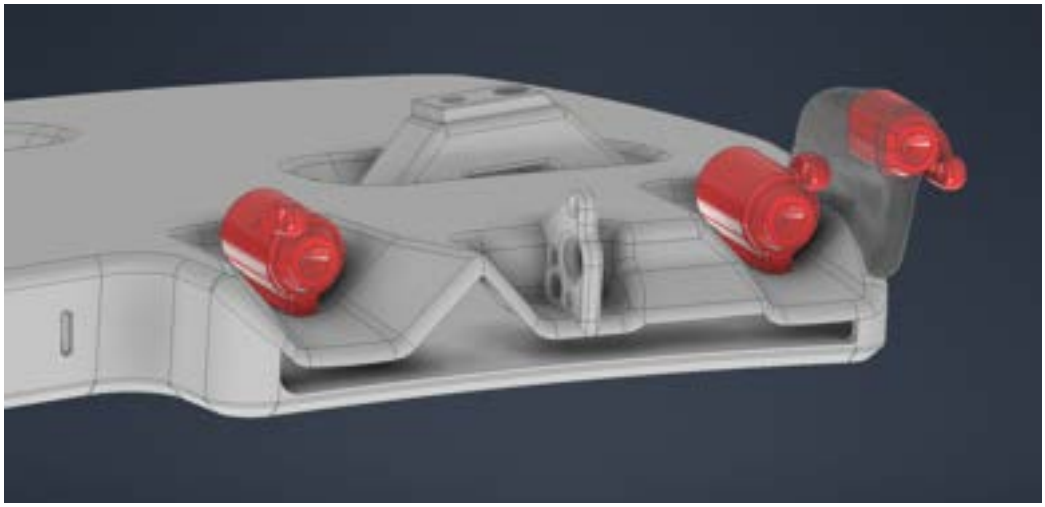

(c) Tooling ball mounts

Figure 13: Main design features of the graph latticed prototype.

(a) Graph Diamond latticed petal (b) TPMS Diamond latticed petal

Figure 14: Final latticed prototype designs.

acquired from the two packages, there was a 2 % difference which was deemed to be acceptable. The prototype geometries were also discretized using shell and beam elements in the AM design software. However, when comparing displacement results it became apparent that shell and beam elements do not provide sufficient accuracy. The final displacement results were acquired using the FEA tool of the AM design software with solid element discretization of the Graph prototype geometry.

Two load cases were examined, loading during the SPDT process and loading during operation. The SPDT process was modelled by applying a uniform pressure load of 3500 Pa to the mirror surface, fixing the dowel pin holes in Uy and Uz, fixing the SPDT contact surfaces in Ux, and applying a force load of 1400 N on each screw hole, equivalent to the load exerted by an M4 screw.[9] The operational load was modeled by applying screw forces on the tooling ball mounts representing the loading of M3 screws. The nodes on the mirror surface were filtered and their displacement was exported as a displacement point map in .CSV format. This displacement point map was imported into a a custom MATLAB script to perform Zernike fitting and plotting of Zernike terms and distortion shapes. The results of the numerical simulations and Zernike analyses can be seen in Figures 15 and 16.

The locations of the SPDT mounting points were optimised to minimise maximum deflection of the optical surface under pressure loading using an iterative approach. However, this approach was using a simplified simulation model. Using the higher fidelity model and the optimised SPDT mount locations resulted in a large maximum displacement result at one of the corners, featured on the left in Figure 15a. A more balanced displacement map is desired with a smaller local maximum, therefore the location of the SPDT mounts might need to be adjusted further in subsequent design iterations. After subtracting the 35 Zernike terms, the displacement map on the right in Figure 15a, shows distinct peaks and troughs at the locations of the two SPDT mounts on the right side of the prototype, suggesting that stress isolation strategy is needed in the future for those SPDT

mounts. As for the operational loading condition, the dominating Zernike term is X tilt, visible on the left side of Figure 16a and in Figure 16b, which can be attributed to a limitation in setting up a realistic boundary conditions. Furthermore, large displacement concentrations can be seen close to the locations of the tooling ball mounts, on the right in Figure 16a, which suggests that future improvements could be focused on enhancing the stress isolation capabilities of these features.

There are numerous limitations to the simulations performed within this study. Due to limited computational resources, the TPMS prototype could not be analyzed. The pressure values are only estimates, and the constraints are idealised and would require further work to validate. Furthermore, the results are only used as predictions of the deformation shapes and not their magnitude.

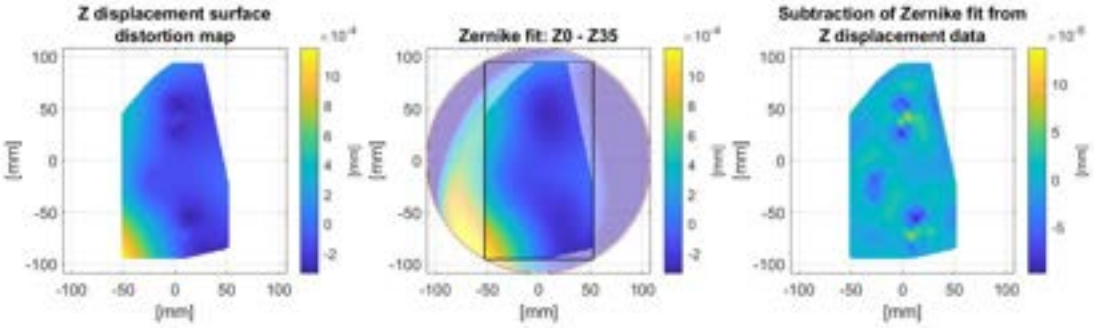

(a) Optical surface form error under SPDT process loading conditions

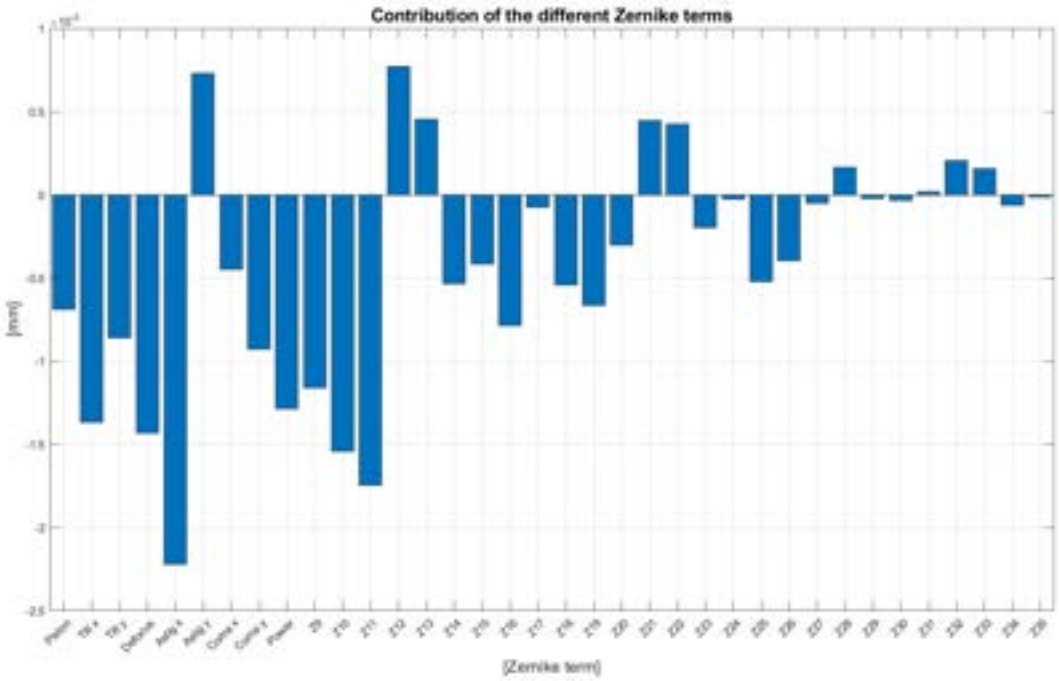

(b) Zernike terms

Figure 15: SPDT loading condition numerical analysis.

4. ADDITIVE MANUFACTURING

Different powders, machines and machine parameters influence the quality of prints for given geometries. In order to better understand this two suppliers were used to print the prototypes. These suppliers were an external

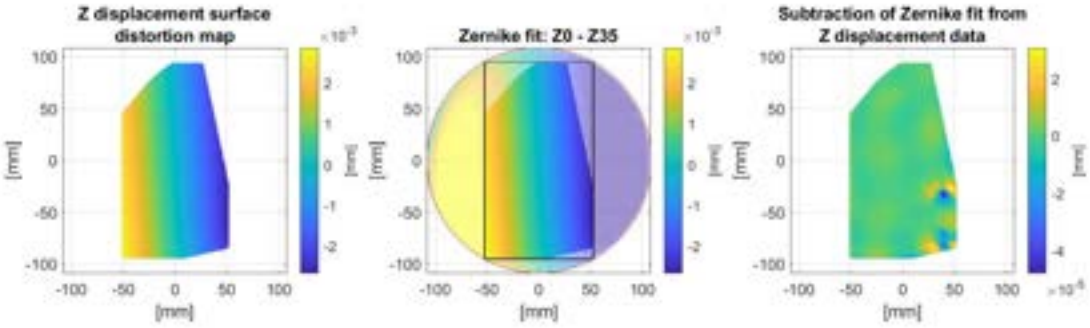

(a) Optical surface form error under screw pressure loading in operation

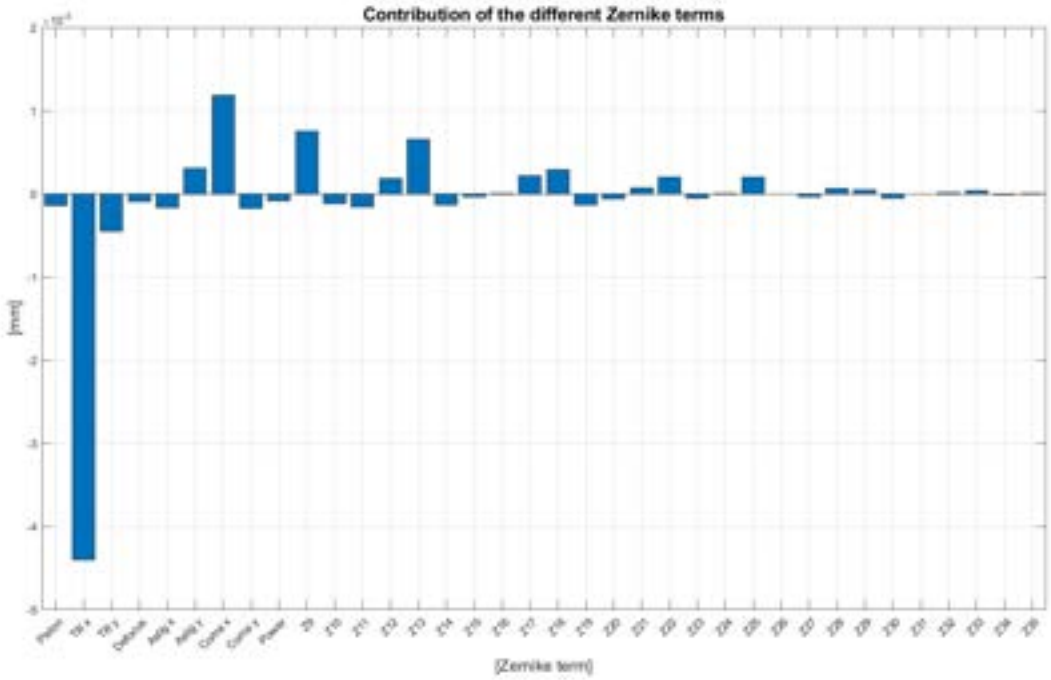

(b) Zernike terms

Figure 16: Operational screw pressure loading condition numerical analysis.

industrial AM bureau operating an SLM 500HL L-PBF printer, and the Henry Royce Institute operating an Aconity Lab printer.

The details of the printer and powder used by the external industrial AM bureau are tabulated in Tables 3 and 4, respectively. Four prototypes were printed in a single batch using this machine, a picture of the printed batch on the build plate is shown in Figure 17. Exact settings of the printing process are unknown due to the commercial production of the prints.

Table 3: Industrial AM Machine parameters.[18]

Parameter	Specification
Name	SLM 500HL
Build envelope	$500 \times 280 \times 320$ mm
Build speed	105 cm^3/h
Laser configuration	4x400 W or 2x(400 W and 1000 W)
Operational beam focus	80–120 µm at 700 nm
Layer thickness	20–200 µm
Scan speed	10 m/s
Inert Gas type	Ar/N2

Table 4: Industrial AM powder parameters.[19]

Parameter	Specification
Material type	AlSi10Mg
Mass density	2.69 g/cm^3
Thermal conductivity at 20 °C	130–150 $W/(m * K)$
Layer thickness	30 µm
Laser power	400 W
Component density	>= 99.5 %
Theoretical build-up rate per laser	24.6 cm^3/h
Particle size	20–63 µm
Particle shape	Spherical

Two Graph prototypes were printed on the research AM machine operated by the Henry Royce Institute in Sheffield. This printer has been used in an earlier study which focused on optimising print parameters with the goal of minimising porosity in the vicinity of surfaces.[10] These custom settings were used during in the printing of the graph prototypes. Table 5 summarises the machine's specifications.

Table 5: Academic AM Machine parameters[9].[20]

Parameter	Specification
Name	AconityLAB
Build envelope	Ø170 mm x H200 mm
Laser configuration	Single mode 400 W / 1000 W
Max scan speed	4 m/s
Optics configuration / Spot size	F-Theta / 80 µm, 3D Scanning / 80–500 µm
Layer thickness	Down to 10 µm

5. POST-MACHINING

After performing surface profilometry on the As-Printed prototypes, the prototypes were sent to the RAL Precision Development Facility for machining using CNC milling and turning machines. The post-machining steps for a single prototype involved laying the petal face down on a small jig-boring machine and skimming the top surfaces of the SPDT mounts; drilling and tapping the screw holes, optically aligning the part and then drilling the dowel pin holes on the SPDT mounts; mounting and aligning the petal onto the machining jig via

Figure 17: Prototypes on the build plate of an SLM 500HL L-PBF machine. Credit: G. Campbell

the SPDT mounts and dowel pin holes; skimming, drilling and tapping the Tooling Ball mounts and rough machining the optical surface on a 3-axis CNC milling machine; balancing the prototype-jig assembly on the SPDT machine; and, finally, perform SPDT machining of the optical surface. An overview of these steps with accompanying renderings can be seen in Figure 18. Pictures taken during the machining process can be seen in Figure 19.

6. METROLOGY

6.1 Surface profilometry

The surface form of the petals printed on the SLM 500HL machine were measured using a Taylor Hobson Talysurf Intra Touch before post-processing. Three 50 mm passes were made on the mirror surface, centered at the axis of rotation for the SPDT process. These measurements were performed to ensure that the ROC was nominally recreated from the .STL files.

Table 6: Surface form measurement results.

Sample	Radius measurements [mm]	Average value [mm]	Deviation [mm]
Graph	669.07 663.75 678.55	670.46	-11.82
TPMS	705.94 709.34 713.87	709.72	27.44

Comparing the measured average ROCs with the prescribed ROC (682.28 mm), the deviation in surface height

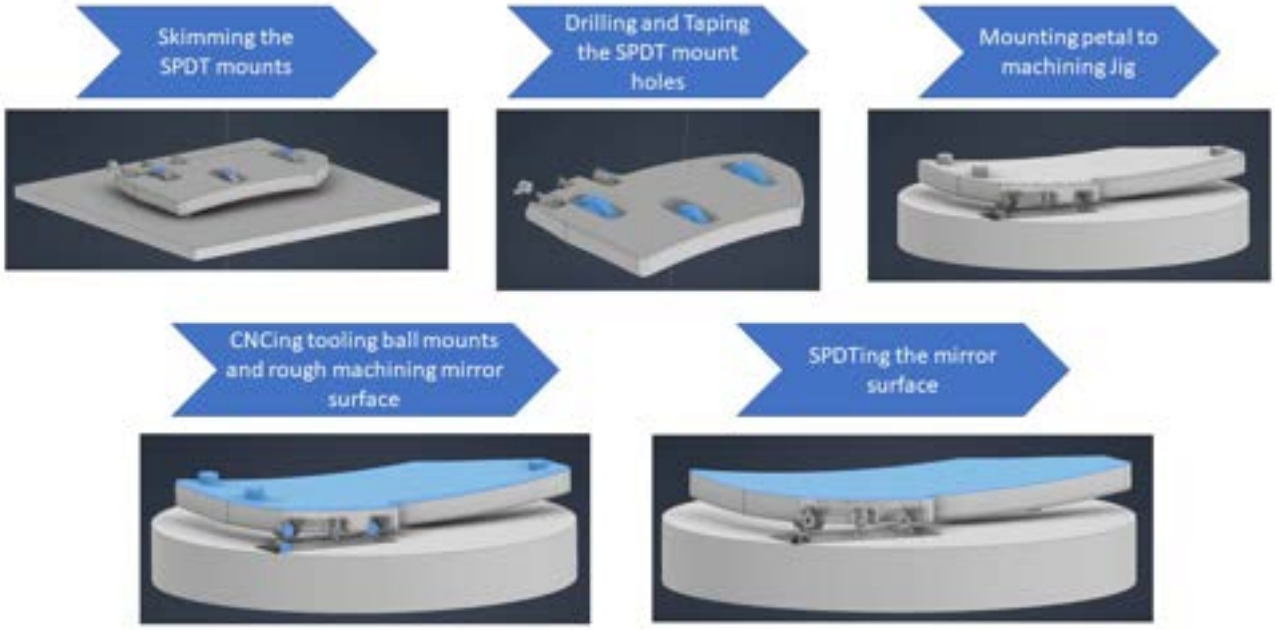

Figure 18: Post-machining steps.

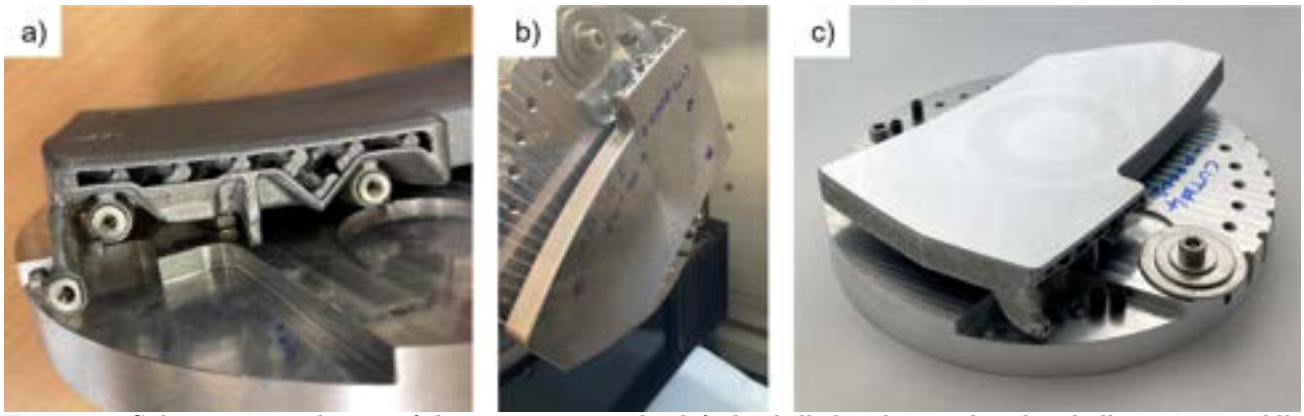

Figure 19: Subtractive machining of the prototype petals: *left* the drilled and tapped tooling ball mounts; *middle* the mirror petal prepared for SPDT; and *right* the generated mirror surface after SPDT.

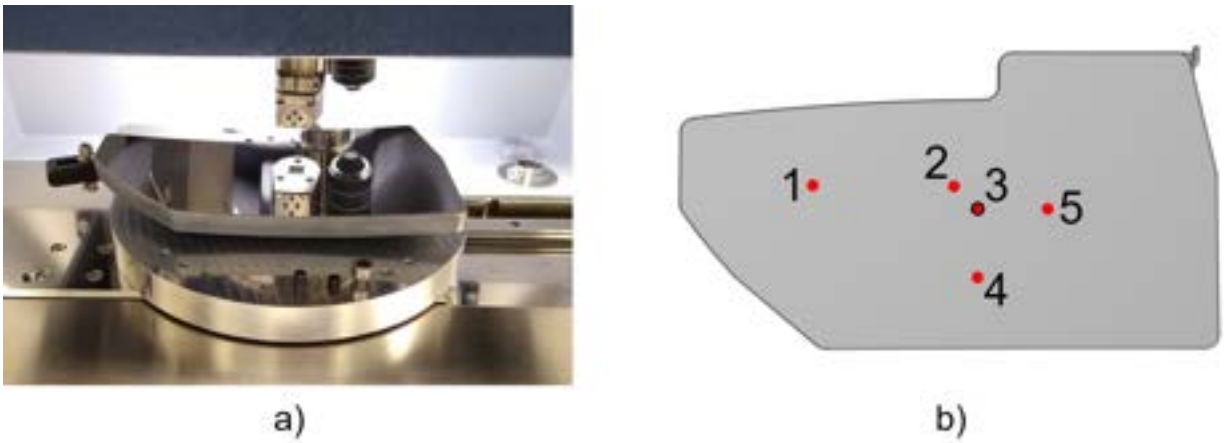

Figure 20: Micro-roughness measurements of the Graph lattice petal: *a)* the Graph petal on the GTX white-light micro-interferometer; and *b)* the numerated ROIs measured, ROI3 represents the centre of SPDT.

is ~ 0.1 mm (Graph) and ~ 0.3 mm (TPMS), this deviation can be corrected within the additional material added to the surface for machining 1.25 mm (Table 1).

6.2 Surface roughness

The surface roughness on the two petals were measured after the surface form using the same instrument with a diamond stylus. The raw data was processed using a Gaussian S-filter $\lambda_s = 8\,\mu$m and a Gaussian L-filter $\lambda_c = 2.5$ mm. Three 12.5 mm long passes were made with 2 mm separation, centered around the centre of rotation of the SPDT process. The results are shown in Table 7 below.

Table 7: Surface roughness measurement results.

Sample	Rp [µm]	Rv [µm]	Rz [µm]	Ra [µm]	Rq [µm]
Graph	29.05	13.83	42.88	5.95	7.98
	34.72	16.03	50.75	6.32	8.60
	23.30	13.86	37.16	5.05	6.63
TPMS	27.73	16.54	44.26	5.55	7.40
	27.21	14.59	41.80	5.53	7.19
	21.67	14.20	35.87	5.50	6.73

Based on the data, the PV value (Rz) is below 50 microns, meaning that more than 50 microns of material needs to be cut through to remove the roughness and create the optical surface. This implies that the surface is relatively smooth and potentially less extra material can be added to the optical surface in subsequent design iterations.

6.3 Micro-roughness

Following the first SPDT cut on the Graph Diamond petal, the reflective surface was evaluated at the Diamond Light Source Ltd using a Bruker Contour GT-X stitching microinterferometer (Figure 20 *a)*). The curvature of the optical design prevented an even sampling across the reflective surface; the regions of interest (ROIs) as measured, are highlighted in Figure 20 *b)*. Three magnifications were used to evaluate the ROIs: $\times 2.5$, $\times 10$ and $\times 50$. Table 8 presents the average (Sa) and RMS (Sq) roughness values for the three magnifications and five ROIs - piston, tip, tilt and a spherical term have been removed from the data. In all ROIs except ROI1, the Phase-Shifting Interferometry (PSI) mode was used, for ROI1 Vertical Scanning Interferometery (VSI) was used due to ROC height variation in the field of view - ROI1 is furthest from the centre of curvature.

The roughness data highlight significant variability for the different ROIs and this is confirmed visually when inspecting the surface, as porosity and SPDT effects are clearly visible. Figure 21 highlights the comparison

Table 8: The average (Sa) and the root mean square areal roughness (Sq).

ROI	×2.5		×10		×50	
	Sa [nm]	Sq [nm]	Sa [nm]	Sq [nm]	Sa [nm]	Sq [nm]
#1*	46.3	157	9.9	28	22.5	74.5
#2	24.3	314	8.4	29.9	5.1	7.3
#3	7.1	11.3	5.6	12.4	5.1	7.0
#4	3.3	4.2	3.1	4.0	2.7	3.8
#5	6.1	33.3	3.3	7.0	4.3	6.9

* measured using VSI rather than PSI.

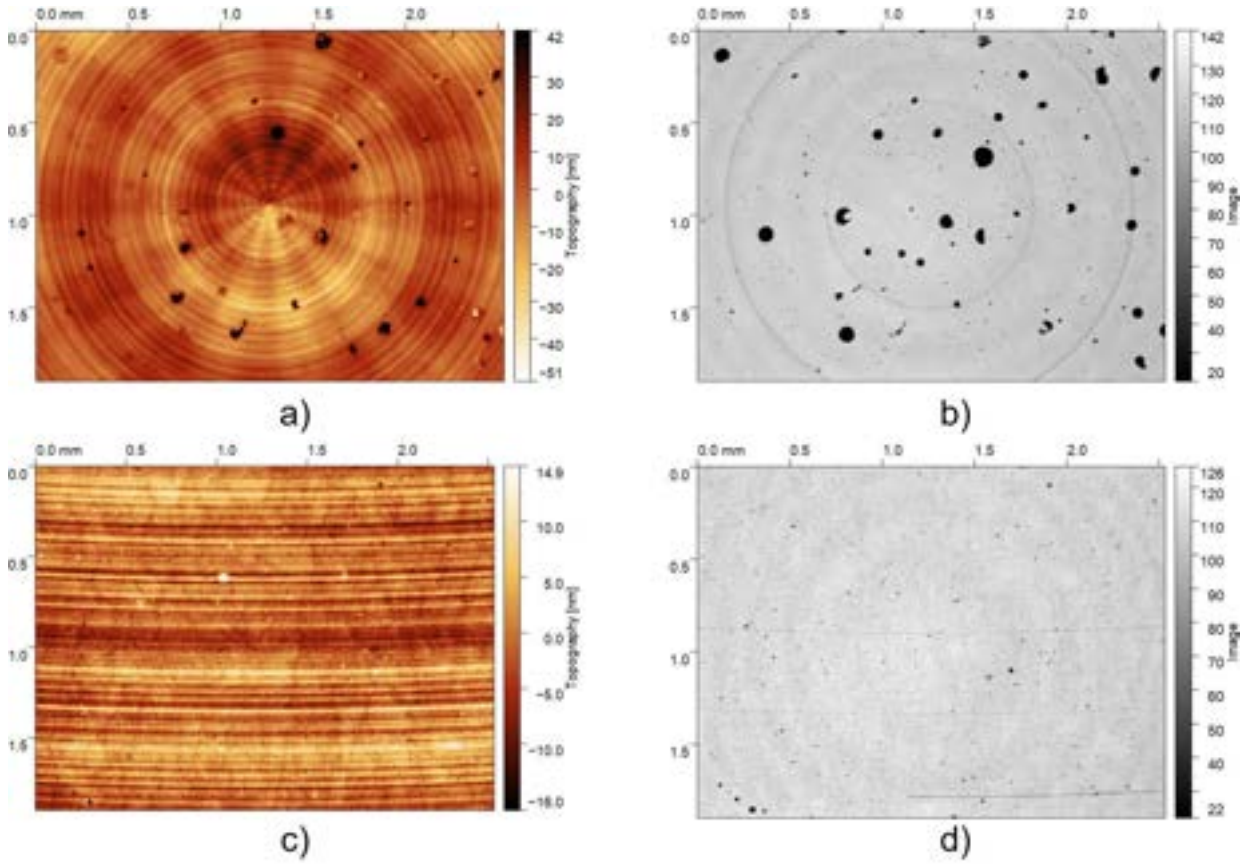

Figure 21: Micro-roughness images (2.5 × magnification) of the Graph lattice petal: *a) & b)* topography and microscope images at ROI3 (the centre of SPDT) respectively; and *c) & d)* topography and microscope images at ROI4 respectively.

between ROI3 and ROI4: ROI3 is located at the centre of SPDT and large circular pores are evident; whereas ROI4 exhibits only a few small pores, which leads to its improved micro-roughness. In ROI3, 'spokes' are seen radiating from the centre of rotation, it is suspected this is an effect caused by balancing the non-symmetric mirror onto the SPDT spindle. The microscope images (Figure 21 *b)* and *d)*) highlight the size and location of the porosity in the topography data. The circularity of the pores suggests that the pores were created through overheating, which has caused pores to form at the bottom of the melt pool, this form of AM porosity is know as keyhole porosity.[10]

Porous reflective surfaces are not desirable and a parallel work stream is investigating methods for reduction.

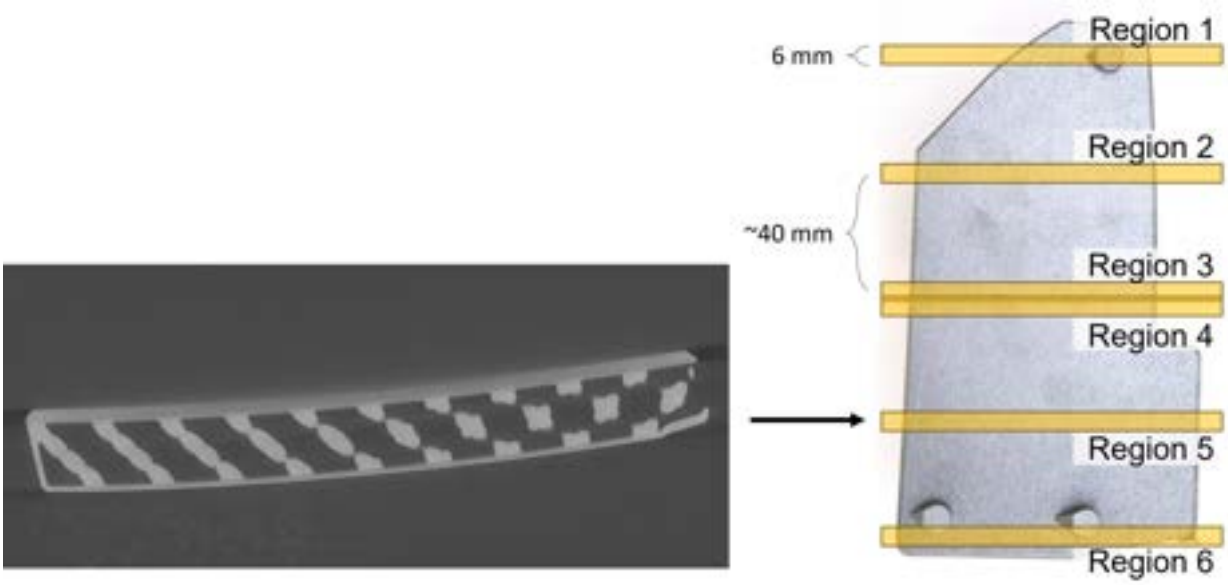

Figure 22: Data extraction for XCT analysis: *left)* an example slice extracted from the Graph prototype, arrow indicates extraction location; *right)* the partition of the prototypes into measurement regions.

The objective of this research was to focus on the design and manufacture, whilst accepting that an external AM bureau would offer a short lead time, but not optimise the print parameters. However, ROI4 does highlight the potential of an AM substrate to generate <5 nm RMS, implying that with the correct AM build parameters and SPDT technique, mirrors for visible to infrared wavelengths, for applications such as ISAAC, are possible.

6.4 X-ray computed tomography

XCT was used to evaluate the internal structure of the as-printed prototype petals. Three datasets were taken from each prototype style, evaluating the prototypes as a whole (1 voxel = 110 µm) and evaluating the prototypes as two halves (1 voxel = 60 µm). The objective of the XCT data was to evaluate the printed substrates for porosity, internal lattice print quality, and conformance to the original STL print file. Due to the recent acquisition of the XCT data, only a limited analysis of porosity has been undertaken.

The 60 µm voxel data was used to explore porosity; the machine settings used were an X-ray tube voltage and current of 150 kV, and 150 µA respectively and a 0.5 mm copper filter. The data from both prototypes were divided into six regions, three from the top half and three from the bottom. Each region contained 100 slices, which represents 6 mm in length, shown in Figure 22. The creation of 6 mm volumes, ensured that the analysis could be undertaken on a non-specialised computer. The analysis focussed on the 2 mm thick substrate where the optical surface would be generated: the concave external face. Dragonfly 2022.2 was used to segment the regions to identify pores within the solid material; segmentation uses a threshold value, where voxel grey values above the threshold indicate one material and grey values below indicating another, for example, aluminium and air. In this initial analysis, the threshold value was calculated using the global Otsu's method, which minimises the intra-class variances between the segmented classes, in this case high- and low-density regions corresponding to the solid material and surrounding air/internal porosity respectively.

Figure 23 highlights how the threshold from Otsu's method has been applied to segment Region 5 into pores (red) and the aluminium structure - the same trend was seen Regions 1 → 4 and 6. The histogram in Figure 23 highlights the frequency of pores against distance normal to the external concave surface (0 mm = external surface, 2 mm = internal surface). However, confidence is low that this is a full description of porosity within the 2 mm substrate and therefore the observed peaks should be approached with scepticism. A limitation of the XCT data is the contrast of the air-aluminium greyscale, which varies visibly in Region 5 from left to right and with depth from the external concave surface (Figure 22 *left*), the impact from the variability is that the global

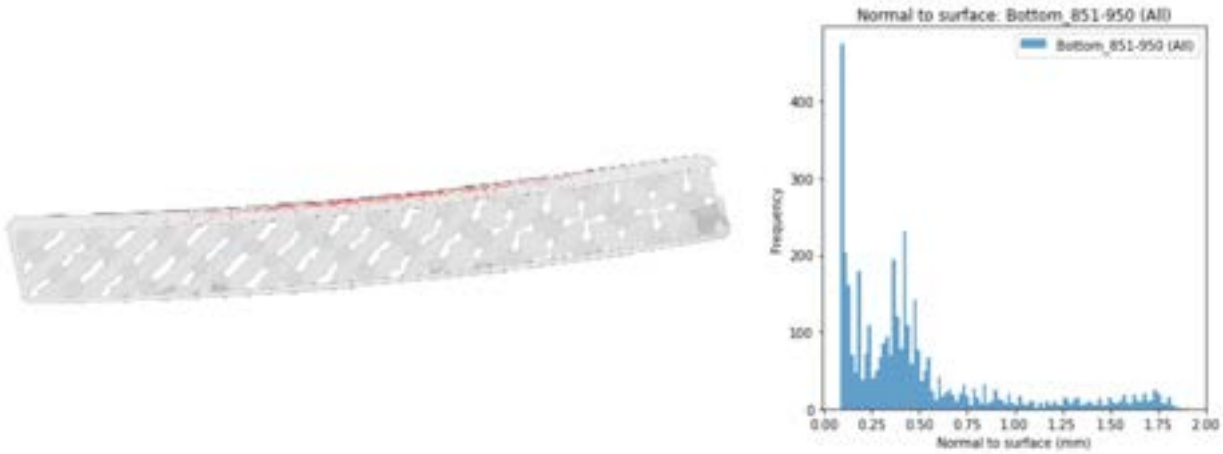

Figure 23: Porosity identified in Region 5 using Otsu's method: *left* porosity (red) plotted relative to location; and *b)* a histogram highlighting the number of pores relative to the normal from the external surface.

Otsu threshold value is inappropriate for accurate segmentation of these XCT data and leads to a non-uniform distribution of porosity (Figure 23 *left*). For example, in Figure 22 *left* the contrast is lower in the centre of the 2 mm substrate than at the edges, which increases the likelihood of an inaccurate definition of the air-aluminium boundary. However, despite the current limitations, future analysis can explore local (adaptive) thresholding methods, which vary the threshold value relative to a localised volume and therefore incorporate the variability in greyscale contrast. Using these local, rather than global methods, it is hoped a more accurate representation of porosity with distance normal to the concave service can be achieved, which in turn could assist in either the upstream AM print parameter definitions, or the downstream subtractive manufacture procedure.

A major limitation of the XCT data for porosity analysis was the voxel size (60 µm). The detection resolution for porosity, that is the smallest pore that can be accurately defined, needs to be greater than at least two times the voxel size, and further, XCT best practice considers single segmented voxels as noise, which lowers the detected porosity seen in Figure 23. From the $\times 2.5$ magnification microscope images in Figure 21, the porosity is well resolved with one pixel equal to ~ 4 µm. Therefore, by using the $\times 2.5$ magnification microscope images within Dragonfly 2022.2 and thresholding using Otsu's method, an indication of the pores that are missing in the XCT images can be estimated. Figure 24 *left* demonstrates how the ROI2 microscope image has been segmented to identify porosity and Figure 24 *right* presents the pore frequency against the 2D equivalent diameter, which is the diameter calculated assuming the pixel area of the pore is circular. Although the 2D equivalent diameter is a poor descriptor for the irregularly shaped pores, it does highlight that the majority of the pores, using $\sim$ 4 µm pixel size, are < 60 µm. This analysis was applied to ROIs 2, 3 and 5, and the percentages of the porosity > 60 µm which are detectable in the XCT data, were 27%, 16% and 6% respectively. It is likely that the 27% measured for ROI2 was affected by the Otsu thresholding of the SPDT scratches.

Future analysis of the XCT data will focus on the macro-structure of the printed prototypes investigating the quality of the printed lattices and the conformance to the STL file. Although the AM print quality (i.e. the porosity) was not an objective of this study, the information gathered from the XCT analysis highlights the importance of appropriate XCT resolution to quantify porosity with confidence. In the production of future prototypes, smaller representative volumes could be destructively extracted from a sacrificial prototype to decrease the voxel size and allow greater confidence in pore identification. If a non-uniform distribution of pores relative to the reflective surface is highlighted then this information can be used to inform an optimum depth for SPDT.

7. SUMMARY AND FUTURE WORK

In this research two types of prototype AM mirrors were developed based on the ISAAC deployable M1 assembly incorporating lightweight lattice structures, topology optimisation and part consolidation. Two lattice types were downselected from an initial set of 33 via automated FEA simulations and powder removal experiments. The

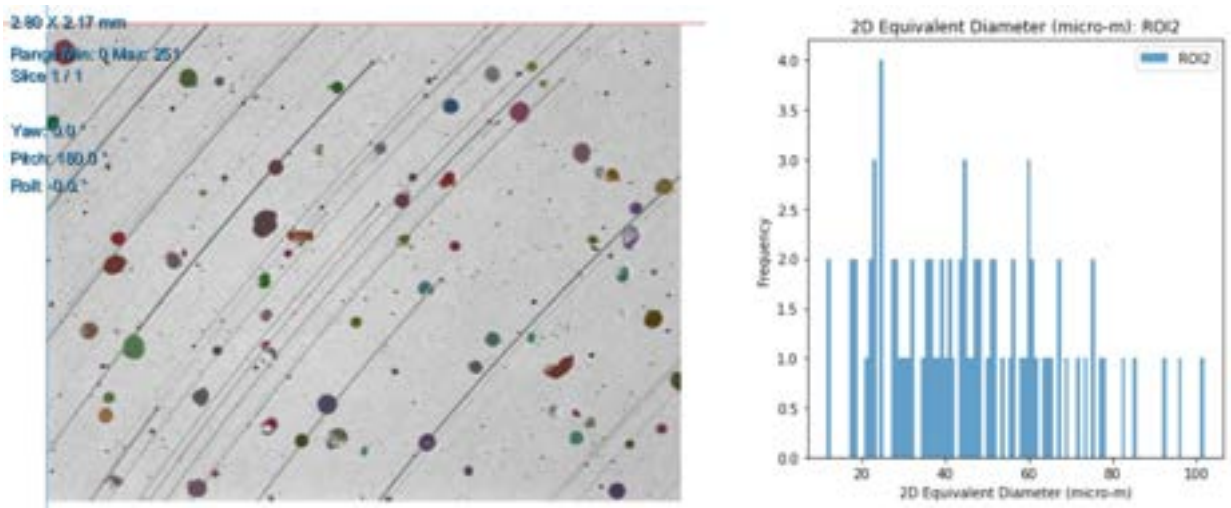

Figure 24: Porosity identified in ROI2 of the microscope images using Otsu's method: *left* the ROI2 microscope image with the identified pores highlighted in colour; *right* a histogram highlighting the number of identified pores and their equivalent diameter in microns.

AM prototypes were developed using DfAM practices and the TPMS version was validated for powder removal using an SLA printed sample. The deformation of the prototypes under post-processing and operational loading was evaluated using FEA and the predicted optical aberrations were determined by Zernike analysis. Multiple prototypes were printed on industrial and academic L-PBF printers to provide a basis of comparison for build quality between different printer strategies and settings.

Future work will include a thorough XCT analysis to evaluate build dimensions and quality, as well as exploring local (adaptive) thresholding techniques for higher confidence porosity analysis; post-processing of a further two aluminium prototypes and exploring the use of hot isostatic pressing to reduce porosity; assembly within the ISAAC test rig to explore deployment; and an evaluation of the optical surface form error using interferometery. A future project could build upon the simulations presented in this paper, and explore the behaviour of latticing with variable thickness and/or cell size, driven by topology optimisation.

8. DATA ACCESS STATEMENT

The as-printed and post-processed STL files presented in this paper are openly available from eData, the STFC Research Data repository, at https://edata.stfc.ac.uk/handle/edata/937.

ACKNOWLEDGMENTS

We wish to acknowledge the support of the Henry Royce Institute for advanced materials for Marcell Westsik through the Student/Researcher Equipment Access Scheme enabling access to Aconity3D AconityLAB facilities at The Royce Discovery Centre at the University of Sheffield; EPSRC Grant Number EP/R00661X/1 & EP/P02470X/1.

The authors acknowledge the UKRI Future Leaders Fellowship 'Printing the future of space telescopes' under grant # MR/T042230/1.

REFERENCES

[1] Atkins, C., van de Vorst, L., Conley, A., Farkas, S., Hugot, E., Mező, G., Morris, K., Roulet, M., Snell, R., Tenegi-Sanginés, F., Todd, I., Vega-Moreno, A., and Schnetler, H., "The OPTICON A2IM cookbook: an introduction to additive manufacture for astronomy," in [*Astronomical Telescopes + Instrumentation*], 121880W, SPIE (2022).

[2] Atkins, C. and van de Vorst, B., [*OPTICON A2IM Cookbook: an introduction to additive manufacture for astronomy*], Zenodo (June 2021). https://doi.org/10.5281/zenodo.5042159.

[3] NASA, "Webb's mirrors." https://jwst.nasa.gov/content/observatory/ote/mirrors/index.html (2022). (Accessed: 2022-08-01).

[4] NASA, "Hubble space telescope - observatory - optics." https://www.nasa.gov/content/goddard/hubble-space-telescope-optics-system (2022). (Accessed: 2022-08-01).

[5] Atkins, C., Brzozowski, W., Dobson, N., Milanova, M., Todd, S., Pearson, D., Bourgenot, C., Brooks, D., Snell, R., Sun, W., Cooper, P., Alcock, S. G., and Nistea, I.-T., "Lightweighting design optimisation for additively manufactured mirrors," in [*Astronomical Optics: Design, Manufacture, and Test of Space and Ground Systems II*], Hull, T. B., Kim, D. W., and Hallibert, P., eds., **11116**, 1111617, International Society for Optics and Photonics, SPIE (2019).

[6] Atkins, C., Brzozowski, W., Dobson, N., Milanova, M., Todd, S., Pearson, D., Bourgenot, C., Brooks, D., Snell, R., Sun, W., Cooper, P., Alcock, S. G., and Nistea, I.-T., "Additively manufactured mirrors for CubeSats," in [*Astronomical Optics: Design, Manufacture, and Test of Space and Ground Systems II*], Hull, T. B., Kim, D. W., and Hallibert, P., eds., **11116**, 1111616, International Society for Optics and Photonics, SPIE (2019).

[7] Breen, C., Walpole, J., Atkins, C., McPhee, S., Cliffe, M., Moffat, J., Edwards-Mowforth, M., Lister, I., Reynolds, L., Conley, A., Allum, S., Snell, R. M., Tammas-Williams, S., and Watson, S., "Outgassing properties of additively manufactured aluminium," in [*Advances in Optical and Mechanical Technologies for Telescopes and Instrumentation V*], Navarro, R. and Geyl, R., eds., **12188**, 121882I, International Society for Optics and Photonics, SPIE (2022).

[8] Tan, S., Ding, Y., Xu, Y., and Shi, L., "Design and fabrication of additively manufactured aluminum mirrors," *Optical Engineering* **59**(1), 013103 (2020).

[9] Paenoi, J., Bourgenot, C., Atkins, C., Snell, R., Todd, I., White, P., Parkin, K., Ryder, D., Kotlewski, R., McPhee, S., Chanchaiworawit, K., Chartsiriwattana, P., Laoyang, A., Kuha, T., Leckngam, A., Buisset, C., Rujopakarn, W., and Poshyachinda, S., "Lightweight, aluminum, mirror design optimization for conventional and additive manufacturing processes," in [*Advances in Optical and Mechanical Technologies for Telescopes and Instrumentation V*], Navarro, R. and Geyl, R., eds., **12188**, 121880U, International Society for Optics and Photonics, SPIE (2022).

[10] Snell, R., Atkins, C., Schnetler, H., Chahid, Y., Beardsley, M., Harris, M., Zhang, C., Pears, R., Thomas, B., Saunders, H., Sloane, A., Maddison, G., and Todd, I., "Towards understanding and eliminating defects in additively manufactured CubeSat mirrors," in [*Advances in Optical and Mechanical Technologies for Telescopes and Instrumentation V*], Navarro, R. and Geyl, R., eds., **12188**, 121880V, International Society for Optics and Photonics, SPIE (2022).

[11] Atkins, C., Feldman, C., Brooks, D., Watson, S., Cochrane, W., Roulet, M., Hugot, E., Beardsley, M., Harris, M., Spindloe, C., Alcock, S. G., Nistea, I.-T., Morawe, C., and Perrin, F., "Topological design of lightweight additively manufactured mirrors for space," in [*Advances in Optical and Mechanical Technologies for Telescopes and Instrumentation III*], Navarro, R. and Geyl, R., eds., **10706**, 107060I, International Society for Optics and Photonics, SPIE (2018).

[12] Hilpert, E., Hartung, J., von Lukowicz, H., Herffurth, T., and Heidler, N., "Design, additive manufacturing, processing, and characterization of metal mirror made of aluminum silicon alloy for space applications," *Optical Engineering* **58**(9), 092613 (2019).

[13] Mici, J., Rothenberg, B., Brisson, E., Wicks, S., and Stubbs, D. M., "Optomechanical performance of 3D-printed mirrors with embedded cooling channels and substructures," in [*Optomechanical Engineering 2015*], Hatheway, A. E., ed., **9573**, 957306, International Society for Optics and Photonics, SPIE (2015).

[14] Al-Ketan, O., Rowshan, R., and Abu Al-Rub, R. K., "Topology-mechanical property relationship of 3d printed strut, skeletal, and sheet based periodic metallic cellular materials," *Additive Manufacturing* **19**, 167–183 (2018).

[15] Meyer, G., Musekamp, J., Göbel, F., Gardian, F., and Mittelstedt, C., "Manufacturability investigation of inclined AlSi10Mg lattice struts by means of selective laser melting," *Manufacturing Letters* **31**, 101–105 (2022).

[16] Ferraro, A., Pirozzi, M., Annacondia, E., and Donato, L. D., "Powder bed fusion/sintering machines: safety at workplaces," *Procedia Manufacturing* **42**, 370–374 (2020). International Conference on Industry 4.0 and Smart Manufacturing (ISM 2019).

[17] Schwartz, N., Brzozowski, W., Ali, Z., Milanova, M., Morris, K., Bond, C., Keogh, J., Harvey, D., Bissell, L., Sauvage, J.-F., Dumont, M., Correia, C., Rees, P., and Bruce, H., "6U CubeSat deployable telescope for optical Earth observation and astronomical optical imaging," in [*Space Telescopes and Instrumentation 2022: Optical, Infrared, and Millimeter Wave*], Coyle, L. E., Matsuura, S., and Perrin, M. D., eds., **12180**, 1218031, International Society for Optics and Photonics, SPIE (2022).

[18] SLM Solutions, "SLM 500HL." https://pdf.directindustry.com/pdf/slm-solutions/slm-500-hl/114591-626988.html. (Accessed: 2023-04-04).

[19] SLM Solutions, "Al-Alloy AlSi10Mg." https://www.camodels.co.uk/wp-content/uploads/2021/01/metal-am-aluminium-alsi10mg-datasheet-ca-models.pdf (2021). (Accessed: 2023-04-04).

[20] Henry Royce Institute, "Powder laser bed melting suite." https://www.royce.ac.uk/equipment-and-facilities/powder-laser-bed-melting-systems/. (Accessed: 2023-06-14).